Solid State Ionics 230 (2013) 77–82

Contents lists available at SciVerse ScienceDirect

Solid State Ionics

journal homepage: www.elsevier.com/locate/ssi

# Synthesis and Raman micro-spectroscopy investigation of $Li_7La_3Zr_2O_{12}$

F. Tietz [a], T. Wegener [a], M.T. Gerhards [a], M. Giarola [b], G. Mariotto [b,*]

[a] Forschungszentrum Jülich, Institute of Energy and Climate Research (IEK-1), D-52425 Jülich, Germany
[b] Dipartimento di Informatica, Università di Verona, I-37134 Verona, Italy

ARTICLE INFO

*Article history:*
Received 30 April 2012
Received in revised form 2 October 2012
Accepted 26 October 2012
Available online 16 November 2012

*Keywords:*
$Li_7La_3Zr_2O_{12}$ solid electrolyte
Synthesis of tetragonal and cubic crystal phases
Polarized Raman micro-spectroscopy

ABSTRACT

The $Li^+$ ion conductor $Li_7La_3Zr_2O_{12}$ was synthesized by solid state reaction as a ceramic with tetragonal and cubic crystal structure. The synthesis parameters were varied for these polycrystalline samples, e.g. the starting materials for Li and Zr, the crucible materials and the thermal treatments. Product formation is sensitive to the $ZrO_2$ starting powder as well as the crucible material due to reactions between the powder mixture and the crucible wall. In this study, only the use of an alumina crucible or the addition of alumina resulted in the successful preparation of cubic $Li_7La_3Zr_2O_{12}$.

For single-crystal preparation, flux growth experiments were carried out at 1000 and 1200 °C either in alumina crucibles lined with a gold foil or in magnesia crucibles and using $Li_2CO_3$ ($Li_2O$) as flux. The small crystals were separated from the solidified flux by washing larger lumps in water. Irrespective of the additions of alumina, only tetragonal micro-crystals of $Li_7La_3Zr_2O_{12}$ were obtained.

These micro-crystals were studied by micro-Raman scattering spectroscopy. Polarized Raman spectra were recorded either in nearly backscattering or 90° geometry. The majority of Raman modes expected for the tetragonal phase (space group $I4_1/acd$, $Z=8$) were satisfactorily displayed. So far, it has not been possible to make unambiguous symmetry assignments of the observed peaks because of the unknown orientation of the micro-crystals.



## 1. Introduction

During the coming decade, renewable energy will receive more widespread application enabling society to become more independent of fossil fuels. The challenges of the efficient use of renewable energy include exploring the possibility of remote, stationary and mobile energy storage. Especially for stationary energy storage, future batteries have to guarantee not only high safety standards with respect to overcharging and deep discharge, but also cycling stability, long life time and operational efficiency. Greater inherent safety may be obtained with solid state batteries which need further development with respect to materials, manufacturing, cell design and dimensions. In the case of solid electrolytes, the recent discovery of new materials with high $Li^+$ ion conduction such as $Li_{10}GeP_2S_{12}$ [1] and $Li_7La_3Zr_2O_{12}$ [2] has generated interest in the development of solid-state batteries and new pathways for combinations of materials. Especially the garnet-type material $Li_7La_3Zr_2O_{12}$ (LLZ) has several advantageous properties such as the ability to be manufactured in air, good thermal and chemical stability to reactions with metallic lithium and environmental compatibility [2].

The results obtained by Murugan et al. [2] proved difficult to reproduce when we attempted to synthesize the high-conductivity phase with cubic symmetry. Meanwhile it is evident that small amounts of alumina or other trivalent cations are necessary to stabilize the cubic structure [3,4], similar to former investigations of Al additions in scandia-stabilized zirconia [5,6]. Here we describe additional synthesis parameters and their impact on phase formation, i.e. the starting materials for Li and Zr, the crucible materials and the thermal treatments. Furthermore, the materials obtained were characterized by a vibrational dynamics investigation to better understand the transport properties of the tetragonal and cubic LLZ without and with additions of alumina, respectively.

## 2. Experimental

### 2.1. Preparation of polycrystals

The starting powder mixture for solid-state reaction was composed of LiOH (Merck, 98%; 2% $Li_2CO_3$), $La_2O_3$ (Treibacher, 99.9%), and $ZrO_2$ (Alfa Aesar, 99.7%). Before mixing in a stoichiometric ratio, LiOH and $La_2O_3$ were dried at 200 and 900 °C, respectively. 10 wt.% of LiOH was added to the powder mixture to compensate lithium oxide loss during sintering as well as 1–5 wt.% $Al_2O_3$ to stabilize the cubic phase of $Li_7La_3Zr_2O_{12}$ (*c*-LLZ). This mixture was subsequently wet-milled in isopropanol with $ZrO_2$ balls until a mean particle size of $d_{50}=0.7$ μm was reached. After drying the milled powder was calcined at 980 °C for 5 h to obtain the tetragonal phase of $Li_7La_3Zr_2O_{12}$ (*t*-LLZ). The *t*-LLZ was then ground and homogenized together with additional 5 wt.% LiOH and uniaxially pressed to pellets with a diameter of 13 mm at a pressure of 260 MPa.

* Corresponding author. Tel.: +39 045 8027031; fax: +39 045 8027068.
*E-mail address:* gino.mariotto@univr.it (G. Mariotto).

0167-2738/$ – see front matter © 2012 Elsevier B.V. All rights reserved.
http://dx.doi.org/10.1016/j.ssi.2012.10.021

The pressed pellets were sintered in air at different temperatures between 980 and 1260 °C for 12 h. Four different crucible materials were used: Pt, $Al_2O_3$, MgO and $ZrO_2$. In addition to the powders mentioned above, the synthesis was also carried out with $Li_2CO_3$ (Sigma Aldrich, 99.99%) and four other $ZrO_2$ powders from different suppliers to investigate the impact of impurities and impurity concentrations on phase formation. The sintered pellets were characterized by X-ray diffraction (XRD) using a Siemens D5000 diffractometer with Cu $K_\alpha$ radiation. Quantitative phase determination was carried out by Rietveld refinement. Whereas the use of $Li_2CO_3$ and LiOH did not show any difference, the $ZrO_2$ powders showed divergent results in phase formation and are reported here in more detail.

### 2.2. Preparation of single crystals

The calcined reaction product (*t*-LLZ) was mixed with the same weight of $Li_2CO_3$ as flux for the crystal growth process [7]. The powder mixture was either filled into alumina crucibles lined with gold foil or into magnesia crucibles. The crucible was heated up to 1000 or 1200 °C, kept at this temperature for 72 h and then cooled down to room temperature at 5 K/min. The crystals were separated from the solidified flux by washing larger lumps in water. The different crystal growth temperatures did not lead to significant differences in size or amount of crystals obtained.

### 2.3. Vibrational spectroscopy measurements

Micro-Raman spectra were recorded under different polarization settings from both pellets of crystallized ceramics and single-crystal samples either in backscattering or in 90° scattering geometry, using a micro-sampling approach. Micro-crystal alignment was obtained by a micro-manipulator. The spectra were excited by the 514.5 nm or 568.2 nm laser line and detected by a CCD (256×1024 pixels), cooled at -134 °C by liquid nitrogen. The scattered radiation was analyzed by a triple monochromator (Horiba-Jobin Yvon, model T64000), set in double subtractive/single configuration and mounting holographic gratings (1800 lines/mm). The spectral resolution was about 0.6 $cm^{-1}$/pixel.

## 3. Results and discussion

### 3.1. Synthesis in different crucible materials

A systematic study of phase formation was carried out with crucibles of $Al_2O_3$, MgO and $ZrO_2$ as it is evident from earlier results that LLZ and the starting powder mixture react with the crucible [4,8].

Increasing the temperature of the heat treatment led to significant differences in product formation. As examples of each crucible material, Fig. 1 shows the X-ray diffraction patterns of the sintered materials at 1200 °C. Using an alumina crucible, *c*-LLZ is formed as the main reaction product with a lattice parameter of a = 12.964(2) Å. Small amounts of $La_2Zr_2O_7$, $La(OH)_3$ (as a hydration product of $La_2O_3$ during storage in ambient air) and $LaAlO_3$ can be detected in the 1–3% range. These small impurities can be avoided by homogenization and repeated grinding and sintering [8]. In the case of MgO as crucible material, pure *t*-LLZ is formed. Although Mg-containing garnets are well known, the possible incorporation of Mg does not lead to a cubic stabilization of the garnet structure. However, the reaction with the crucible walls was less pronounced than that resulting from an alumina crucible. The use of zirconia crucibles was explored because no additional element would then be involved in the synthesis. Although a reaction with the starting powder mixture can be expected, it was not clear which reaction path and to what extent the reaction with the crucible wall will take place. If the crucible material reacts with the excess of Li-containing precursors forming $Li_2ZrO_3$ without affecting garnet formation, $ZrO_2$ crucibles could be a less expensive option for crystal growth experiments with LLZ. However, the use of $ZrO_2$ crucibles cannot be recommended, because a strong and irreversible reaction with $La_2O_3$ to $La_2Zr_2O_7$ was observed, which increases steadily with temperature. This reaction effectively minimizes the La content in the oxide mixture and garnet formation is suppressed.

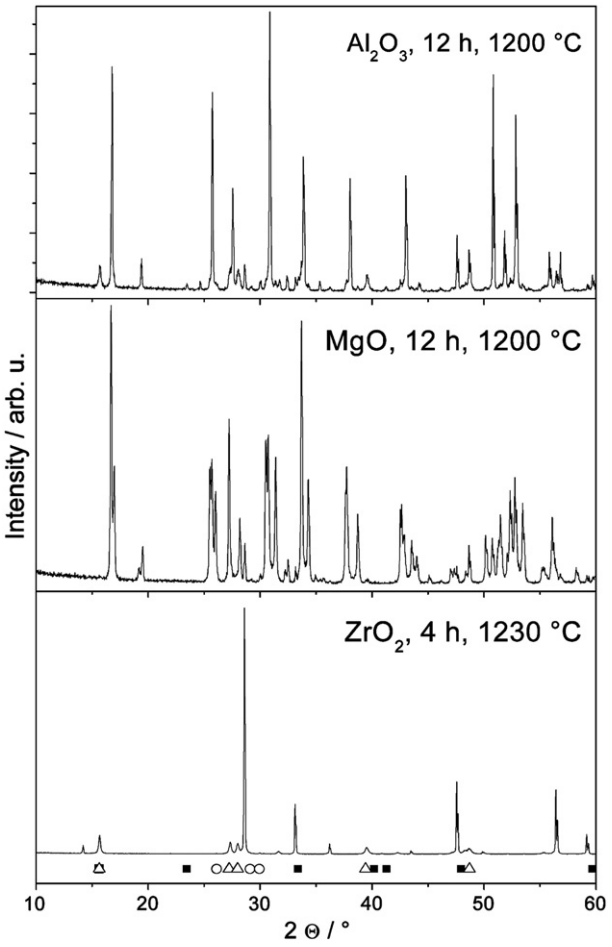


**Fig. 1.** XRD patterns of phases formed after sintering in different crucible materials: Top: $Al_2O_3$ crucible (12 h at 1200 °C), middle: MgO crucible (12 h at 1200 °C) and bottom: $ZrO_2$ crucible (4 h at 1200 °C). The main constituent in the XRD patterns is *c*-LLZ (filled diamonds), *t*-LLZ (filled circles) and $La_2Zr_2O_7$ (filled squares), respectively. Reflections of detected secondary phases are indicated by open circles ($LaAlO_3$), open triangles ($La(OH)_3$), and hatched circles ($La_2Li_{0.5}Al_{0.5}O_4$).

The influence of the addition of alumina on the solid-state reaction was verified by sintering experiments using crucible materials as having little impact on phase formation. For this purpose calcined Al-free *t*-LLZ was sintered in the Pt and MgO crucibles at 1200 °C for 12 h. In the same way a *t*-LLZ pellet containing 1 wt.% $Al_2O_3$ was also sintered in a MgO crucible. Whereas the Al-free samples showed only the XRD pattern of *t*-LLZ, the latter sample with $Al_2O_3$ revealed the *c*-LLZ phase.

### 3.2. Synthesis at different temperatures

In this series of experiments, sintering took place in an $Al_2O_3$ crucible and the temperature was varied between 1000 and 1240 °C. The amount of *t*-LLZ steadily decreased with increasing temperature and was completely converted to *c*-LLZ at 1200 °C (Fig. 2). It is interesting to note that $La_2Zr_2O_7$ is first formed at 1040 °C, but shows a fluctuating content of 3–5% with increasing temperature up to 1200 °C, at which temperature only a very small amount could be detected. By increasing the temperature further to 1240 °C, the *c*-LLZ decomposed mainly to $La_2Zr_2O_7$ and $LaAlO_3$, but also $Li_2ZrO_3$ and $LiAlO_2$ are formed.

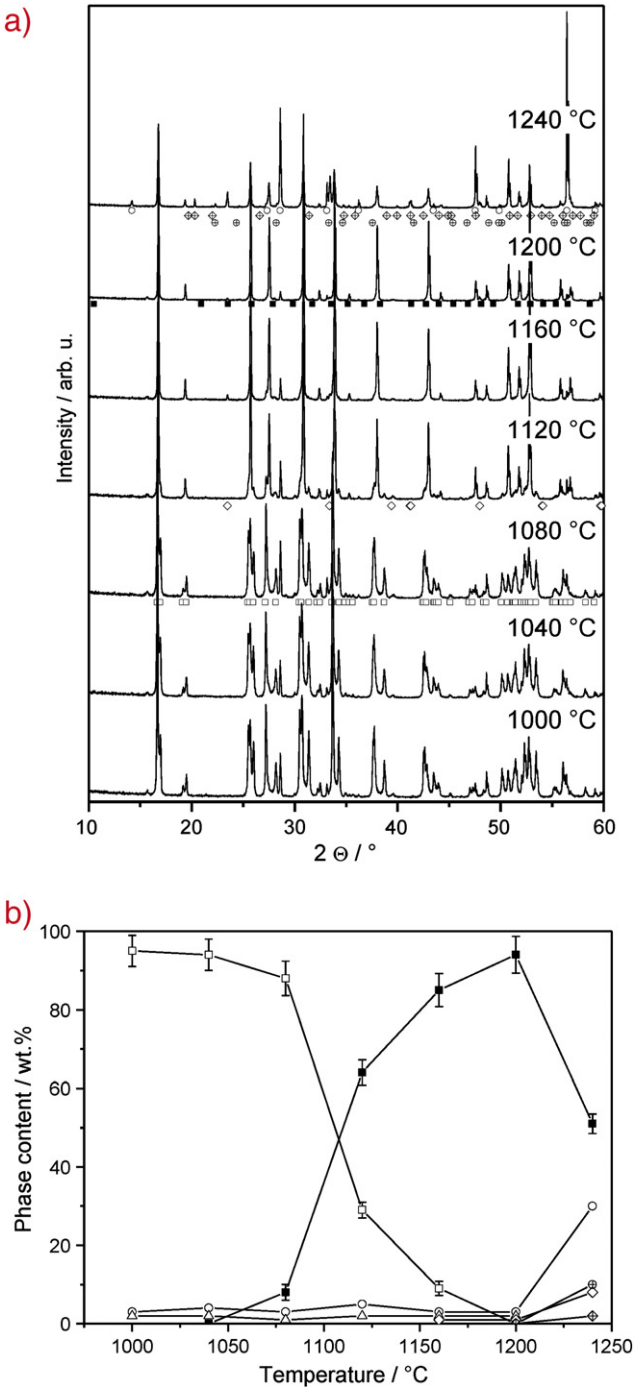


**Fig. 2.** a) XRD patterns of phases formed after sintering at different temperatures in an $Al_2O_3$ crucible (dwell time 12 h at each temperature), b) temperature-dependent occurrence of phases determined by Rietveld refinement: open squares = *t*-LLZ, filled squares = *c*-LLZ, open circles = $La_2Zr_2O_7$, open diamonds = $LaAlO_3$, hatched diamonds = $Li_2ZrO_3$, hatched circles = $LiAlO_2$.

### 3.3. Synthesis with different Zr-containing starting materials

In this series of experiments, it was tried to determine the influence of starting chemicals, especially their impurities, on the phase formation of LLZ. Therefore the following zirconia powders with varying purity levels were used during synthesis:

1) $ZrO_2$ (Alfa Aesar, 99.7%) as reference (see Sections 3.1 and 3.2)
2) $ZrO_2$ (Strem Chemicals, >99%)
3) $ZrO_2$ (UCM Advanced Ceramics, High Purity Zirconia, >99%)
4) $ZrO_2$ (Yingkou Imerys Astron Chemicals, 98.7%)
5) $ZrO_2$ (UCM Advanced Ceramics, Engineering Grade Zirconia).

Before calcination, the starting powder mixture was milled to the same particle size distribution to avoid interfering results from different grain sizes. Therefore the particle size distribution for all batches was kept constant at the following characteristic values: $0.42<d_{10}<0.50$ μm, $0.68<d_{50}<0.72$ μm and $0.98<d_{90}<1.15$ μm. After calcination at 980 °C all samples only contained *t*-LLZ, and only the batch with $ZrO_2$ no. 3 showed minor amounts of monoclinic $Li_6Zr_2O_7$.

After sintering at 1200 °C in an $Al_2O_3$ crucible, in all cases *c*-LLZ was formed as the main crystallographic phase, but differences in the appearance of secondary phases were detected. The observed phases and the main impurities (>100 ppm) for each $ZrO_2$ quality are listed in Table 1. In all five LLZ samples $La_2Zr_2O_7$, $La_2O_3$ (or $La(OH)_3$ as a hydration product formed during storage) and $LaAlO_3$ were detected in slightly different amounts. Besides these impurity phases also $La_2Li_{0.5}Al_{0.5}O_4$ and $Li_{1.82}ZrO_3$ appear as additional phases in the samples with $ZrO_2$ no. 2, no. 5 and no. 3, respectively.

Apart from Ce, Th and U, the impurities listed in Table 1 can all be incorporated in the garnet structure, which makes it difficult to interpret the influences of individual elements. Various elements can even occupy different crystallographic sites as in the very well-known yttrium aluminum garnet (YAG) or yttrium iron garnet (YIG) and the site occupancy of an individual element mainly depends on the cations involved. However, as a general trend those elements which usually occupy tetrahedral sites in the garnet structure (here Mg, Al, Ti, and Fe) can be regarded as substituents for Li. They do not show a clear tendency of preferred formation of secondary phases. Impurity elements which preferably occupy octahedral sites (Mg, Al, Ti, Cr, Fe, Zn, Dy-Yb, and Hf), lead to a reduced formation of additional zirconates and seem to be dissolved in the LLZ. $ZrO_2$ powders with higher amounts of impurity elements preferably occupying dodecahedral sites in the garnet (Na, Ca, Fe, Cd, and Dy-Yb) also seem to form smaller amounts of secondary phases. Obviously, such elements are incorporated in the garnet and do not induce secondary phase formation. $ZrO_2$ nos. 4 and 5 showed the highest total amounts of impurities resulting in the smallest amounts

**Table 1**
Main impurities (in ppm) and secondary phases formed after synthesis at 1200 °C in an $Al_2O_3$ crucible. Only impurities with more than 100 ppm are listed.

| Element | $ZrO_2$ No. 1 | $ZrO_2$ No. 2 | $ZrO_2$ No. 3 | $ZrO_2$ No. 4 | $ZrO_2$ No. 5 |
|---|---|---|---|---|---|
| Na | 119 | 333 | 309 | 329 | 296 |
| Mg | 127 | 260 | 379 | 345 | 503 |
| Al | 178 | 633 | | 5076 | 4903 |
| Ca | 513 | 825 | 1224 | 3910 | 3308 |
| Ti | | 396 | | 1088 | 568 |
| V | | | | | 175 |
| Fe | 146 | 483 | | 648 | 521 |
| Zn | 227 | 386 | 789 | 624 | 494 |
| Ba | | | | 227 | |
| Ce | | | | 534 | 344 |
| Nd | | | | 94 | |
| Dy | | 108 | | 213 | 125 |
| Er | | 132 | | 218 | 140 |
| Yb | | 570 | | 962 | 434 |
| Hf | 161 | 13,342 | 16,959 | 10,963 | 11,537 |
| Th | | | | 236 | |
| U | | | | 1360 | 589 |
| *Secondary phases (in wt.%)* | | | | | |
| $La_2Zr_2O_7$ | 10 | 2 | 3 | 5 | 3 |
| $La_2O_3 + La(OH)_3$ | 3 | 1 | 4 | 2 | 2 |
| $LaAlO_3$ | 2 | 1 | 2 | 1 | 1 |
| $La_2Li_{0.5}Al_{0.5}O_4$ | | 1 | | | 1 |
| $Li_2ZrO_3$ | | | 1 | | |
| *t*-LLZ | <10 | 10–20 | <5 | <5 | <5 |

of impurity phases thus indicating that the additional elements contribute to a stabilization of the *c*-LLZ phase.

### 3.4. Synthesis of single crystals

Fig. 3a shows a 100 μm crystal with a few smaller twin-grown crystals on the rear. As shown here, the crystals can be effectively cleaned in water and no flux material remains on the crystal surfaces. The La:Zr ratio determined by SEM/EDX as well as the crystal habitus revealed that this example is a LLZ garnet crystal. It is definitely a *t*-LLZ crystal, because no alumina was added to the initial powder mixture and the Raman scattering showed splitting of Raman modes (see below). Directly after crystal growth the crystals are covered with an approx. 2 μm layer of the flux (Fig. 3b). In order to identify the elements, the right-hand side of Fig. 3b is shown as a back-scattering image. Here the light gray pyramidal particles mainly contain La and Zr whereas the black areas in between are composed of non-scattering Li. This image gives an insight into the growth mechanism of the crystals. As such surface coverage can also be observed during synthesis of polycrystalline samples due to the excess LiOH or $Li_2CO_3$ in the powder mixture, this raises questions about the reliability of conductivity measurements on such samples. It is likely that the thick "grain boundaries" contribute significantly to the conductivity. In a preliminary test, a washed powder showed a lower conductivity than an as-prepared powder after pelletizing and sintering of both specimens.

So far no cubic single crystals have been found in the fluxes although the necessary requirements (Al content and similar synthesis temperature as for polycrystalline materials) were adopted. Further experiments are necessary to better understand the reasons for the discrepancy in product formation during preparation of polycrystalline and single-crystal samples.

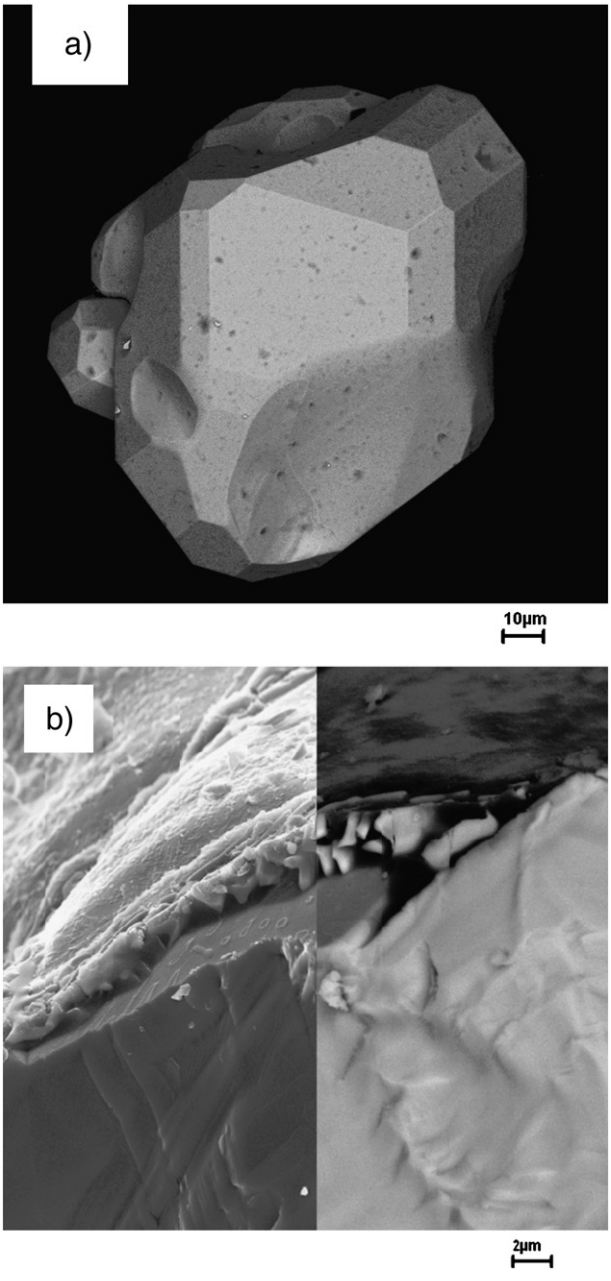


**Fig. 3.** a) SEM image of a crystalline *t*-LLZ monolith of some tens of μm. b) Fractured crystal with crystal surface before cleaning in water (left-hand side: secondary electron image, right-hand side: back-scattering electron image).

### 3.5. Raman spectroscopy

Unpolarized micro-Raman spectra obtained in backscattering geometry from polycrystalline pellets of *t*-LLZ after calcination at 1100 °C in a Pt crucible, and of *c*-LLZ sintered at 1200 °C in an $Al_2O_3$ crucible are plotted in Fig. 4. The figure clearly evidences the overall similarity between the spectra of the two different crystal structures, which are characterized by the same sort of atomic/ionic local environment, and, therefore, the vibrational frequencies must be practically the same. However, the Raman spectrum of *t*-LLZ presents a higher number of spectral features (peaks or bands) than that of the cubic phase, due to either the more distorted arrangement of $Li^+$ ions [7] or the lower symmetry of the tetragonal garnet-related structure. As for the observed general broadening of the Raman bands of *c*-LLZ, especially in the low-wave number region, a not-negligible contribution should be related to either static or dynamic disorder of highly mobile $Li^+$-ions migrating along the isotropic pathways connecting the different

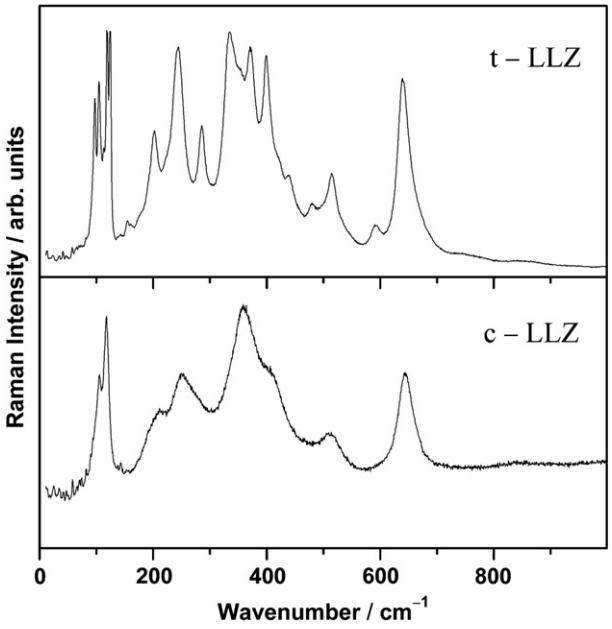


**Fig. 4.** Unpolarized micro-Raman spectra obtained in backscattering geometry from polycrystalline pellets of *t*-LLZ, after calcination at 1100 °C in a Pt crucible, and of *c*-LLZ, sintered at 1200 °C in an $Al_2O_3$ crucible.

allowed sites within this structure. In spite of the different number of spectral features shown by the *t*-LLZ and *c*-LLZ structures, their Raman spectra can be divided into three regions, as is usually done for silicate garnets [9,10], i.e.: a low-energy region below about 300 $cm^{-1}$, an intermediate-energy region between 300 and 550 $cm^{-1}$, and a high-energy region above 550 $cm^{-1}$. The high frequency region shows the vibrational stretching modes of $ZrO_6$ octahedral units, while the intermediate region mainly consists of vibrational bending modes of the octahedral units, and, finally, the low-frequency region contains translational modes of mobile cations. In particular, the intermediate-energy region of *c*-LLZ exhibits some broad, partly overlapping bands associated to degenerate Raman modes, which turn out partly splitted in *t*-LLZ phase, due to its lower symmetry, thus originating a higher number of observed peaks. Similar behavior is observed for the two bands in the low-energy region just above 100 $cm^{-1}$, where the two narrow bands of *c*-LLZ peaking at about 107 $cm^{-1}$ and 121 $cm^{-1}$ split, in turn, into two very sharp component lines peaking at about 100 and 108 $cm^{-1}$, and 121 and 127 $cm^{-1}$, respectively. However, no reliable symmetry assignment can be attempted on the basis of the spectra obtained from either ceramic pellet with tetragonal or cubic crystal structure, due to the random orientation of their micro-domains.

In order to derive the symmetry assignment of the Raman active modes of garnet-type LLZ, a careful and detailed polarization analysis of its Raman spectrum should be carried out from a single-crystal. For this purpose polarized micro-Raman spectra from the main, apparently flat region of the *t*-LLZ crystalline monolith, shown in Fig. 3a, were recorded either in the backscattering geometry or at the 90° scattering angle by using a micro-manipulator to orient the crystal under the microscope objective, used for the collection of scattered radiation, and the experimental data, obtained under three different polarizations, are plotted in Fig. 5. According to Scott and Porto [11], in a typical experiment in 90° scattering geometry the incident laser beam travels along a crystallographic axis, the polarization of the incident light is coincident with a second axis and the scattered radiation is collected along the third. Therefore, in terms of XYZ axes of the laboratory frame, parallel polarization is X(YY)Z, while crossed polarization is referred to as X(YX)Z.

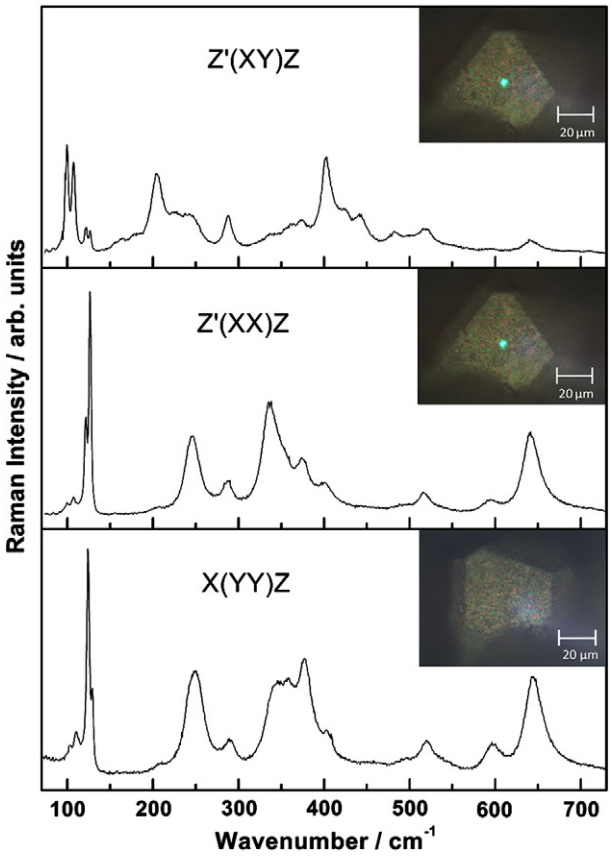


**Fig. 5.** Typical micro-Raman spectra recorded under different polarizations from a *t*-LLZ micro-crystal in both 180° and 90° scattering geometries. Polarization labels refer to the laboratory frame axes XYZ (with $Z' = -Z$).

We recently adopted this approach, by combining a proper scattering geometry with an accurate orientation of the single crystal, to carry out a very thorough study of the vibrational dynamics of orthophosphate single crystals with zircon structure (space group: $I4_1/amd$), which allowed the selection of all 12 independent components of the Raman tensor of this tetragonal structure, in complete agreement with the group theoretical prediction for this tetragonal structure [12].

In the past, the same procedure has been extensively exploited to study the vibrational spectra of garnet single crystals of different compositions and sizes, with defined crystallographic orientation [9,10,13,14]. In fact, in the case of garnet with cubic symmetry (space group: Ia–3d), group theory predicts the occurrence of twenty five Raman active modes, i.e. $3A_{1g} + 8E_g + 14T_{2g}$. [15]. For measurements in the standard 90° scattering geometry, if the crystal is properly oriented according to its crystallographic axes, $A_{1g}$ and $E_g$ modes of the garnets are found to be polarized parallel to the laser polarization (parallel polarization or X(YY)Z in the laboratory frame) while the $T_{2g}$ modes are polarized perpendicular to the laser polarization (crossed polarization or X(YX)Z in the laboratory frame).

However, in the case of a small single micro-crystal, as it is here for the *t*-LLZ crystal, an accurate study of its vibrational dynamics requires a micro-manipulator to preliminarily orient the sample so that its crystallographic axes properly match the polarization direction of the incident laser beam. So, for instance, by means of this integrated approach it has been recently possible to carry out from a single micro-crystalline domain of a natural anatase $TiO_2$ crystal a full polarization analysis of its Raman spectrum, and to definitely resolve the vibrational dynamics of this $TiO_2$ crystal structure. In fact, exploiting the anisotropy of this crystalline structure, a nearly perfect alignment of its crystallographic axes with the laboratory axes was achieved during the Raman measurements and, therefore, an accurate selection of all the independent components of its polarizability tensor was obtained. In this way, two nearly degenerate Raman modes of the anatase $TiO_2$ [16] were properly resolved and definitively assigned in symmetry.

Unfortunately, in the case considered here, the orientation of the *t*-LLZ micro-crystal was not straightforwardly achievable, so that it was not possible to observe the Raman spectra of pure symmetry. In spite of this, by exploiting some different polarization settings in the laboratory frame, we were able to satisfactorily contrast most of the expected Raman modes of $A_{1g}$, $E_g$ or $T_{2g}$ symmetry for the tetragonal phase of LLZ (space group $I4_1/acd$, $Z = 8$). Fig. 5 shows the typical micro-Raman spectra observed under three different polarization settings. The bottom panel of Fig. 5 shows the parallel polarized X(YY)Z spectrum obtained in 90° scattering geometry from the *t*-LLZ micro-crystal, preliminarily oriented by means of the micro-manipulator so that an edge is perfectly aligned with the laser polarization direction. The middle panel of the same figure displays the parallel polarized Z′(XX)Z spectrum obtained in 180° scattering geometry from the same single crystal, after a 45° rotation around the axis Z, perpendicular to its main face, as shown in the inset of the same panel. Finally the top panel shows the spectrum obtained in the same scattering geometry under crossed Z′(XY)Z polarization. The wavenumbers of all the Raman modes observed from the *t*-LLZ crystalline monolith are listed in Table 2, together with those observed on *c*-LLZ pellets. A tentative symmetry assignment for most of the *t*-LLZ Raman modes is also reported in the first column of this table.

**Table 2**
Energy ($cm^{-1}$) and symmetry assignments of Raman modes of tetragonal and cubic LLZ.

| Symmetry (tentative) | *t*-LLZ ($cm^{-1}$) | *c*-LLZ ($cm^{-1}$) |
|---|---|---|
| $T_{2g}$ | 100 | |
| $T_{2g}$ | 108 | 107 |
| $E_g$ | 122 | 121 |
| $E_g$ | 127 | |
| $T_{2g}$ | 157 | 144 |
| $E_g$ | 183 | |
| $T_{2g}$ | 206 | 209 |
| $T_{2g}$ | 228 | |
| $A_{1g}$ | 246 | 251 |
| $T_{2g}$ | 288 | |
| $E_g$ | 336 | |
| | 356 | |
| $T_{2g}$ | 362 | 361 |
| $A_{1g}$ | 376 | |
| $E_g$ or $T_{2g}$ | 402 | 410 |
| $T_{2g}$ | 425 | |
| $E_g$ | 442 | |
| $T_{2g}$ | 484 | |
| | 496 | |
| $T_{2g}$ or $E_g$ | 517 | 514 |
| $E_g$ | 595 | |
| $A_{1g}$ | 642 | 645 |
| $T_{2g}$ | 712 | |

## 4. Summary

The $Li^+$ ion conductor $Li_7La_3Zr_2O_{12}$ was synthesized as a ceramic with a tetragonal and cubic garnet-like structure by solid-state reaction.

For single-crystal preparation, flux growth experiments were carried out at 1000 and 1200 °C either in alumina crucibles lined with a gold foil or in magnesia crucibles and using $Li_2CO_3$ ($Li_2O$) as flux. The small crystals were separated from the solidified flux by washing larger lumps in water. Irrespective of the addition of alumina only tetragonal micro-crystals of $Li_7La_3Zr_2O_{12}$ were obtained.

Micro-Raman spectra of LLZ pellet samples in tetragonal and in cubic symmetry give clear evidence of the different $Li^+$-ion arrangements in the two crystal phases.

Polarized micro-Raman spectroscopy on tetragonal LLZ micro-crystals allows us to selectively contrast several Raman modes and to carry out a tentative assignment in terms of their symmetry.

## Acknowledgments

Financial support from the German Federal Ministry of Education and Research (BMBF) under contract no. 13N9973 (Kompetenzverbund Nord) is gratefully acknowledged. M. Giarola received financial support from the Regione Veneto within the Programma Operativo FSE 2007–2013. The authors thank M. Ziegner for XRD measurements and data analysis, and Dr. D. Sebold for SEM investigations.

## References

[1] N. Kamaya, K. Homma, Y. Yamakawa, M. Hirayama, R. Kanno, M. Yonemura, T. Kamiyama, Y. Kato, S. Hama, K. Kawamoto, A. Mitsui, Nat. Mater. 10 (2011) 682.
[2] R. Murugan, V. Thangadurai, W. Weppner, Angew. Chem. Int. Ed. 46 (2007) 7778.
[3] T. Yoshida, A. Honda, Y. Sato, European patent application, EP 2 159 867 A1 2009.
[4] C.A. Geiger, E. Alekseev, B. Lazic, M. Fisch, Th. Armbruster, R. Langner, M. Fechtelkord, N. Kim, Th. Pettke, W. Weppner, Inorg. Chem. 50 (2011) 1089.
[5] Y. Mizutani, M. Tamura, M. Kawai, O. Yamamoto, Solid State Ionics 72 (1994) 271.
[6] F. Tietz, W. Fischer, Th. Hauber, G. Mariotto, Solid State Ion. 100 (1997) 289.
[7] J. Awaka, N. Kijima, H. Hayakawa, J. Akimoto, J. Solid State Chem. 182 (2009) 2046.
[8] H. Buschmann, J. Dölle, S. Berendts, A. Kuhn, P. Bottke, M. Wilkening, P. Heitjans, A. Senyshyn, H. Ehrenberg, A. Lotnyk, V. Duppel, L. Kienle, J. Janek, Phys. Chem. Chem. Phys. 13 (2011) 19378.
[9] A.M. Hofmeister, A. Chopelas, Phys. Chem. Miner. 17 (1991) 503.
[10] B.A. Kolesov, C.A. Geiger, Phys. Chem. Miner. 25 (1998) 142.
[11] J.F. Scott, S.P.S. Porto, Phys. Rev. 161 (1967) 903.
[12] M. Giarola, A. Sanson, A. Rahman, G. Mariotto, M. Bettinelli, A. Speghini, E. Cazzanelli, Phys. Rev. B 83 (2011) 224302.
[13] J.P. Hurrell, P.S. Porto, I.F. Chang, S.S. Mitra, R.P. Bauman, Phys. Rev. 173 (1968) 851.
[14] J.J. Song, P.B. Kein, R.L. Wadsack, M. Selders, S. Mroczkowski, K. Chang, J. Opt. Soc. Am. 63 (1973) 1135.
[15] J. Koningstein, O. Sonnich Mortensen, J. Mol. Spectrosc. 27 (1968) 343.
[16] M. Giarola, A. Sanson, F. Monti, G. Mariotto, M. Bettinelli, A. Speghini, G. Salviulo, Phys. Rev. B 81 (2010) 174305.